



Systematic approach to process parameter optimization for laser powder bed fusion of low-alloy steel based on melting modes

Simon Bergmueller¹ · Lukas Gerhold¹ · Lorenz Fuchs¹ · Lukas Kaserer¹ · Gerhard Leichtfried¹

Received: 12 January 2023 / Accepted: 2 April 2023
© The Author(s) 2023

Abstract

In the metal additive manufacturing (AM) process of laser powder bed fusion (LPBF), there are a limited number of materials suitable for producing parts with high density and desired mechanical properties. To establish novel materials, it is essential to determine optimized process parameters in order to overcome process-related challenges and mitigate defects such as lack of fusion, keyholing, and balling. Scaling laws based on thermophysical properties and process parameters can be used to transfer knowledge from other materials or LPBF systems. In this work, a scaling law is used to adjust process parameters for single-track experiments over a wide range, which are laser power P_L (100–1000 W), scan speed v_s (300–2500 mm/s), and laser spot size d_s (0.08–0.25 mm). Compared to existing studies, the parameter range is thus extended towards large laser spot sizes and high laser powers. The scaling law used is based on the calculation of the normalized enthalpy $\frac{\Delta H}{h_s}$. The ratio of the deposited energy density ΔH and the melting enthalpy h_s correlates with the dimensions of the melt pool. According to the aspect ratio δ_c of the melt pool of each single track, the respective melting mode—conduction, transition, and keyhole mode—was identified. The process parameters of the single tracks in transition mode were used to optimize the density of the LPBF specimens with varying hatch distance h_d (0.06–0.12 mm), resulting in specimens with a relative density of > 99.8%. The proposed methodology can accelerate the process parameter finding for new alloys and avoid process-related defects.

Keywords Laser powder bed fusion (LPBF) · Melting mode · Low-alloy steel · Additive manufacturing (AM) · Laser parameter optimization · Normalized enthalpy

1 Introduction

Laser powder bed fusion (LPBF) is an additive manufacturing (AM) process that is particularly suitable for producing metallic components with high demands for mechanical properties and geometric complexity [1]. Steels, in particular, have great potential because of their good mechanical properties and reasonable price performance. So far, only a limited number of high-alloy steels have been established for the LPBF process, such as 316L, 17 4 PH, and 1.2709 [2–4]. Therefore, it is essential to qualify additional materials for the LPBF process whose properties cover a wide range of applications and are reliable to process [5]. Boehler's E185

is a low-alloy steel that covers a wide range of mechanical properties and can be explicitly adjusted by heat treatment using hot isostatic pressing (HIP), quenching, or nitriding. In addition, it can be processed without substrate plate heating via LPBF and was developed specifically for AM [6, 7]. An advantage of LPBF production of E185, in addition to the freedom to design complex geometries, is the exceptionally high strength, hardness, and elongation in the as-built condition due to the process-related fine microstructure. E185, with its comparatively low alloying element content, has the potential to be used in price-sensitive applications such as the automotive industry [8, 9]. The availability of optimized LPBF parameters supports the introduction of new materials into the associated industrial sectors. In this work, LPBF parameters are assigned to the resulting melting mode based on single-track experiments without powder. Seede et al. have already shown that single-track experiments can be used to determine LPBF parameters and avoid defects that can be attributed to the melting modes that occur [10, 11]. The variation in the

✉ Simon Bergmueller
Simon.Bergmueller@uibk.ac.at

¹ Universität Innsbruck, Faculty of Engineering Sciences,
Department of Mechatronics, Materials Science
Technikerstrasse 13, 6020 Innsbruck, Austria

parameters was previously based on the line energy density (LED) or volume energy density (VED) approach [12]. The melting mode can be determined from the cross-sections of the single tracks. Patel et al. [13] have determined the melting modes in LPBF based on the shape of the melt pool to heat conduction mode, transition mode, and keyhole mode. It has been shown that dimensionless numbers or normalized dimensions are valuable for estimating the effects of parameter variation in LPBF [13–15]. In addition, this can be an effective method for translating LPBF processing parameters from one material to another in order to mitigate process-related defects [5, 16].

In laser welding, the model of normalized enthalpy is utilized to predict the threshold to keyhole mode with the calculation of the deposited energy density and the dependence on process parameters (laser power P_L , scan speed v_s , and laser spot diameter d_s), physical material properties (absorptivity A , thermal diffusivity D , melting enthalpy h_s , with $h_s = \rho \cdot c_p \cdot T_m$, the density ρ , the heat capacity c_p , melting temperature T_m [17, 18]. In scaling laws for LPBF, material-specific models for the energy input and the melting modes are used based on the normalized enthalpy, which is the ratio of the deposited energy density ΔH and the melting enthalpy h_s [19–21].

$$\frac{\Delta H}{h_s} = \frac{A \cdot P_L}{h_s \cdot \sqrt{\pi \cdot D \cdot v_s \cdot \left(\frac{d_s}{2}\right)^3}} \quad (1)$$

In this work, a systematic approach was used to investigate the melt pool shapes of single tracks of the low-alloy steel E185 for different process parameter combinations. Based on a scaling law using the normalized enthalpy $\frac{\Delta H}{h_s}$ the process parameters laser power P_L , scan speed v_s , and laser spot diameter d_s were varied. The melt pool shapes of the single tracks were classified, and an optimized parameter window was specified. In addition to the scaling law, further optimization of parameters, including hatch distance h_d with respect to density, is carried out by producing LPBF bulk samples. With these optimized parameters, LPBF specimens were produced for measuring the tensile strength, elongation, and hardness in both the as-built and heat-treated conditions.

The approach presented here is intended to provide a straightforward framework for quickly specifying LPBF process parameters for new alloys. Thereby, the parameter range has been extended toward a larger laser spot size and higher laser power. With E185, low-alloyed martensitic steel has been chosen, which has only recently been introduced to the market

and has an interesting potential for a broad application in the LPBF field.

2 Materials and methods

2.1 Powder feedstock and its characterization

The material used is the gas-atomized powder E185 from Boehler (Voestalpine BOEHLER Edelstahl GmbH & Co KG, Austria). The chemical composition of the powder was determined by inductively coupled plasma optical emission spectrometry (ICP-OES) by the manufacturer Boehler and is listed in Table 1.

2.2 Single-track experiments and melt track analysis

A customized AconityMIDI LPBF system (Aconity3D, Germany) equipped with one 400 W and one 1000 W Nd-YAG laser from IPG (IPG Laser GmbH, Germany), both lasers with variable spot size d_s , was used for the experiments. As process gas, argon was used, and the oxygen content in the build chamber was kept below 20 ppmv for all experiments. A solid cylindrical part of E185, with $\varnothing 80 \times 10$ mm, was produced with process parameters according to the literature [6]. This part was machine-ground and used as a substrate plate for the single-track experiments (Fig. 1).

For the single-track experiments, the following process parameters were varied: laser power P_L , laser scan speed v_s , and laser spot diameter d_s . A total of 120 single tracks were produced within the process parameter range, as shown in Table 2. The tracks were lasered into the substrate plate without using powder, each along a line with a scan vector length of 10 mm. The 120 tracks were produced twice to ensure reproducibility, as shown in Fig. 1. Tracks 1 to 30 were produced with increasing laser power P_L from 100 to 390 W, track numbers 31 to 60 with increasing scan speed v_s from 300 to 1750 mm/s, and track numbers 61 to 90 with increasing laser spot diameter d_s from 0.08 to 0.25 mm, while the other parameters were kept constant in each case. A narrow range of the normalized enthalpy according to Eq. (1) was used to select process parameters for tracks 91 to 120.

D , ρ , c_p , and T_m are material parameters that were kept constant in this investigation. A was also approximated as constant with 0.4 in the chosen parameter range of the single-track experiments, with reference to King et al., as the investigation did not comprise deep keyholing. For the calculation of the

Table 1 Chemical composition E185 according to voestalpine BOEHLER Edelstahl GmbH & Co KG, Austria

Element	Fe	C	Ni	Cr	Mn	Si	Mo	V
wt.-%	bal	0.19	1.25	0.95	0.30	0.22	0.20	0.15

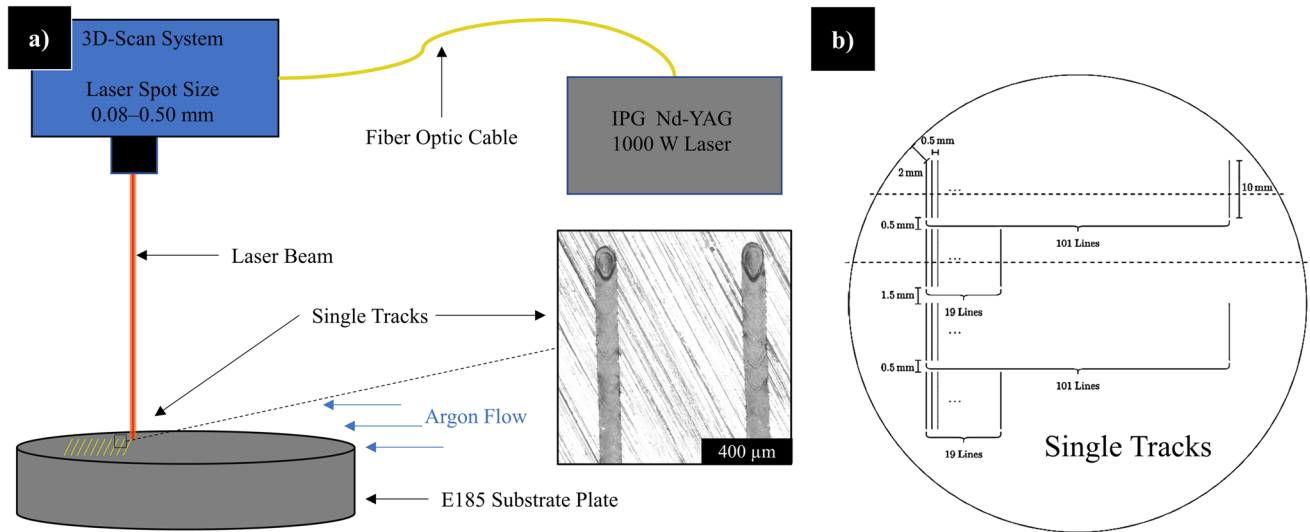


Fig. 1 a Schematic illustration of the experimental setup of the single-track experiments b Arrangement of the single tracks on the E185 LPBF substrate plate. The tracks were duplicated to ensure reproducibility

normalized enthalpy, $D = 5.38 \times 10^{-6} \left(\frac{m^2}{s}\right)$, $\rho = 7893 \left(\frac{kg}{m^3}\right)$, $c_p = 461 \left(\frac{J}{kgK}\right)$, and $T_m = 1773(K)$ were used [22]. Equation (2) splits the normalized enthalpy given in Eq. (1) into a material-dependent part kept constant and a part with machine parameters.

$$\frac{\Delta H}{h_s} = \frac{A \cdot P_L}{\rho \cdot c_p \cdot T_m \cdot \sqrt{\pi \cdot D \cdot v_s} \cdot \left(\frac{d_s}{2}\right)^3} = \frac{A}{\rho \cdot c_p \cdot T_m \cdot \sqrt{\pi \cdot D}} \cdot \frac{P_L}{\sqrt{v_s} \cdot \left(\frac{d_s}{2}\right)^3} \quad (2)$$

It should be noted that the latent enthalpy ΔH_m is not included in Eq. (2) for this low alloy steel and may need to be considered for other materials in the LPBF in addition to the melt enthalpy $h_s = \rho \cdot (c_p \cdot T_m + \Delta H_m)$ [16, 23].

The solid cylindrical part with the single tracks was separated from the build plate by wire erosion and cut into smaller specimens orthogonal to the single tracks to investigate the cross-sections. The embedded specimens were ground with 80- to 2400-grit sandpaper according to standard metallographic procedures and then polished with a 3- or 1- μm diamond suspension (Struers, Germany). For light optical microscopy (LOM) and the measurement of the width and height of the melt tracks and the examination

of the polished cross-sections, an optical focus variation microscope (FVM), InfiniteFocusG4 from Alicona (Bruker Alicona, Alicona Imaging GmbH, Austria), was used at $\times 50$ and $\times 100$ magnification. Etching was done with Nital (4% alcoholic nitric acid, 20 s, dip etching). The scanning electron microscope (SEM) used to make the micrographs was an FEI Quanta 200F FEG-SEM. A Vickers hardness test (HV1) of the cross-section of the single tracks and the substrate plate was performed using the microhardness tester device HMV-G from Shimadzu (Shimadzu, Japan).

Figure 2a shows a schematic representation of a cross-section of a single track as seen in the LOM micrograph. During process-related rapid cooling, the austenitic phase was transformed into martensite. This fact must be considered when measuring the cross-section of a single track. The actual dimension of the melt pool differs from the zone that appears bright in the etched LOM image (Fig. 2b), as everything that appears bright is untempered martensite, while the darker areas are tempered martensite. The untempered martensite includes the melt pool area and the part of the heat-affected zone (HAZ) where the temperature has exceeded the austenitizing temperature and can thus be retransformed to untempered martensite. The actual melt pool boundary

Table 2 Range of process parameters P_L , v_s , and d_s , and of the resulting normalized enthalpy $\frac{\Delta H}{h_s}$ used for the single-track experiments

Single-track numbers	Laser power P_L (W)	Scan speed v_s (mm/s)	Laser spot diameter d_s (mm)	Normalized enthalpy $\frac{\Delta H}{h_s}$
1–30	100–390	600	0.08	7.7–30
31–60	210	300–1750	0.08	9.5–22.9
61–90	250	800	0.08–0.25	3.0–20
91–120	450–1000	1500–2500	0.110–0.185	11.5–15.1

The boldfaced entries are the range of varied parameters

has a smaller extension and is offset radially inward, as shown in the red dashed lines in Fig. 2a and b. Figure 2c shows an SEM backscatter electron (BSE) image of the same single track as in Fig. 2b, where the melt pool boundary can be seen. For this reason, the dimensions e and d_m are corrected, and a corrected aspect ratio $\delta_c = \frac{e_c}{d_c}$ can be obtained, which is used for further evaluation. The actual width of the melt track d_c can be measured with the FVM from the surface due to the elevation of the melt track from the substrate plate. The difference from the d_m measured in the cross-section was used to obtain the correction value $y_c (d_c = d_m - 2 \cdot y_c)$. It is assumed that the HAZ is radially symmetric and that the lateral extent is the same as in the Z direction: $y_c = z_c$. The depth of the single tracks e measured with the LOM in the cross-section was corrected by $z_c (e_c = e - z_c, \text{ see Fig. 2a})$.

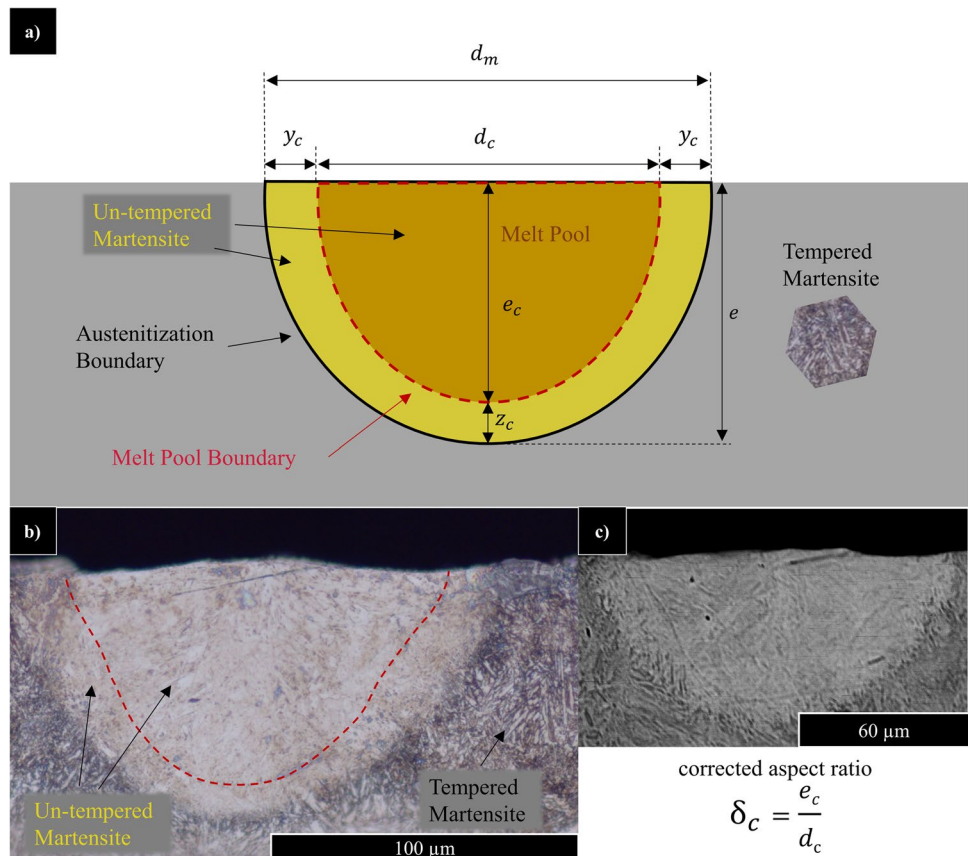
Figure 3 shows the LOM micrograph of the etched and polished single-track cross-sections. Inconsistent morphologies are evident, and the classification of the tracks is based on the ratio of depth to width of the melt pool [13]. Figure 3a shows the heat conduction mode with a $\delta_c < 0.5$. Single tracks with an aspect ratio of $0.5 < \delta_c < 0.8$ are classified as transition mode (Fig. 3b). An aspect ratio $\delta_c = 0.8$ or higher is referred to as keyhole mode, as shown in Fig. 3c. Some of

the single tracks exhibited discontinuities in the melt pool and bulges or undercutting (see Fig. 3d) in the cross-section and were classified as balling defects in accordance with previous work [11, 13, 24].

2.3 LPBF study and characterization

The production of LPBF specimens was conducted with the AconityMIDI. The suitable process parameter ranges for the LPBF study were derived from the results of the single-track studies. A comparison of the parameter range of the single-track experiments and the selected narrower parameter ranges used for the LPBF study is given in Table 3. For the LPBF study, the same process atmosphere conditions as that of the single-track experiments were used, applying argon as a process gas and keeping the oxygen content below 20 ppmv. The tensile and cubic density specimens were produced with a nominal layer thickness t_1 of 0.03 mm, and the hatch pattern was rotated 67° for each layer. A stripe strategy with scan vectors in a meandering sequence (zig-zag) with vector lengths of 5 mm was used, and the hatch distance h_d varied between 0.06 and 0.12 mm. All specimens were separated from the substrate plate by wire erosion cutting. A relative density measurement was performed on all

Fig. 2 Measurement of the cross-section of the single tracks. **a** Schematic representation of the zones and dimensions of the untempered martensite within the austenitization boundary, and the melt pool within the melt pool boundary, as well as the dimensions depth e and diameter d_m with the respective corrected values d_c and e_c . **b** LOM micrograph with the melt pool boundary outlined in red. **c** The same single track as in b in SEM BSE mode, revealing the melt pool boundary



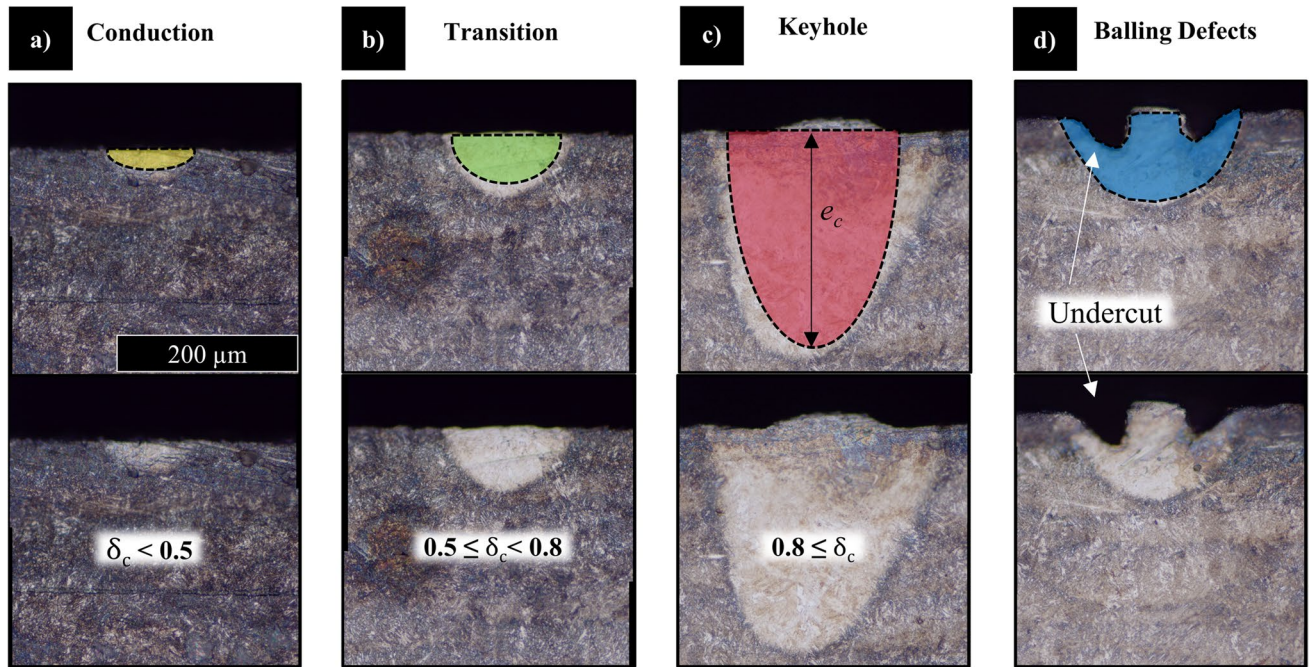


Fig. 3 LOM micrographs of the etched cross-sections of the single tracks. Based on the corrected ratio of the melt pool $\delta_c = \frac{e_c}{d_c}$ the melt

tracks are classified into: **a** heat conduction mode with a $\delta_c < 0.5$, **b** transition mode $0.5 \leq \delta_c < 0.8$, and **c** keyhole mode with $0.8 \leq \delta_c$. **d** Single tracks in which undercuts or balling occur

cube-shaped samples (10×10×10 mm) using Archimedes’ principle. At least three specimens were prepared for the density measurement and tensile tests. Six tensile specimens were heat treated after LPBF production according to the manufacturer’s datasheet, consisting of austenitizing at 850 °C for 30 min, quenching in water, tempering at 200 °C for 2 h, and cooling in air.

Ambient temperature tensile tests were performed using the universal testing machine SHIMADZU AGS-50kNX (Shimadzu, Japan) and polished as-built flat tensile specimens according to DIN 50,125–E 4×8×65 mm. The load was applied perpendicular to the direction in which the specimens were built. A Vickers hardness test (HV1) was performed according to DIN ISO 6507 using the microhardness tester device HVM-G from Shimadzu (Shimadzu, Japan). Three hardness values were averaged for each case.

3 Results

3.1 Powder feedstock properties

Table 4 lists the D_{10} , D_{50} , and D_{90} values and the bulk density, tap density, Hausner ratio, and flowability. Figure 4 shows a scanning electron microscope (SEM) image of the as-delivered E185 powder. Figure 4a is an SEM micrograph in secondary electron (SE) mode showing the powder with different-sized, mostly spherical, powder particles. However, a small fraction of deformed particles and some attached satellites exist. Figure 4b shows a particle in a detailed view with attached satellites in a high-resolution image. An SEM image of a polished cross-section was taken in backscattered electron (BSE) mode (Fig. 4c) to reveal the inside of the powder particles. Figure 4d shows the magnified

Table 3 Process parameters varied in single-track experiments and the LPBF study

	Laser power P_L (W)	Scan speed v_s (mm/s)	Laser spot diameter d_s (mm)	Hatch distance h_d (mm)	Scan strategy	Scan vector length (mm)	Layer thickness t_l (mm)	$\frac{\Delta H}{h_s}$
Single-track experiments	100–1000	300–2500	0.08–0.25	-	Lines	10	-	3.0–30.0
LPBF study	130–260	500–1100	0.08	0.06–0.12	Stripes	5	0.03	9.3–14.8

Table 4 The results of powder characterization of the as-delivered E185 powder: the characteristic diameters of the particle size distribution (PSD) and the measurement of bulk density, tap density, and flowability

	D10 (μm)	D50 (μm)	D90 (μm)	Bulk density (kg/m^3)	Tap density (kg/m^3)	Hausner ratio	Flowability (g/s)
E185	18.9 ± 0.2	30.6 ± 0.4	49.9 ± 0.5	4.17 ± 30	4.68 ± 340	1.12	18.02 ± 2.51

cross-section of a representative particle without internal porosity.

3.2 Melting modes

Figure 5 shows the corrected aspect ratio $\delta_c = \frac{e_c}{d_c}$ of the cross-sections of the single tracks in dependence on the normalized enthalpy $\frac{\Delta H}{h_s}$. The parameter combinations that result in single tracks with a $\delta_c < 0.5$ were assigned to the conduction mode and marked in yellow in Fig. 3a and with yellow triangles in the diagram in Fig. 5. Single tracks in the transition mode ($0.5 \leq \delta_c < 0.8$) were marked in green (Fig. 3b) and with green squares (Fig. 5). Single tracks with δ_c of 0.8 or higher were assigned to the keyhole mode and marked red in Figs. 3c and 5, respectively. Figure 5 reveals a linear relationship between δ_c and the normalized enthalpy $\frac{\Delta H}{h_s}$. Confirming linearity, linear regression yielded a coefficient of determination of $R^2 = 96.47\%$. From the residuals—the deviation of the estimated aspect ratio from the linear

relationship—an analysis of variance was performed, which showed that there were no significant differences between the groups with a test statistic (F) of 1.055 and the associated P value of 0.353. The within-group variance was 0.002 in the conduction mode, 0.001 in the transition mode, and 0.066 in the keyhole mode.

Figure 6 shows an overview of the process parameter combinations of the single-track experiments in different views with the corresponding classification based on the melting mode (C yellow triangles, T green squares, and K red checks). Single tracks with the features of balling, as indicated in Sect. 2.2, are given with blue circles. Figure 6a shows the typical plot with laser power P_L versus scan speed v_s . All scan speeds with $v_s > 1200$ mm/s lead to balling. The same process parameter combinations can also be seen in Fig. 6b, where laser power P_L is plotted versus laser spot diameter d_s . Diameters larger than 0.1 mm lead to single tracks in conduction mode or balling. The laser spot diameter d_s versus scan speed v_s diagram in Fig. 6c shows the conduction mode for

Fig. 4 SEM images of the E185 powder. **a** Powder particles in secondary electron (SE) mode, predominantly spherical and in size according to the measured PSD (Table 3). **b** Spherical particle in SE mode, revealing solidification structures and attached satellites at the particle surface. **c** Polished powder section in SE mode, where no internal porosity is visible in the powder particles. **d** Polished particle in BSE mode without visible inner porosity

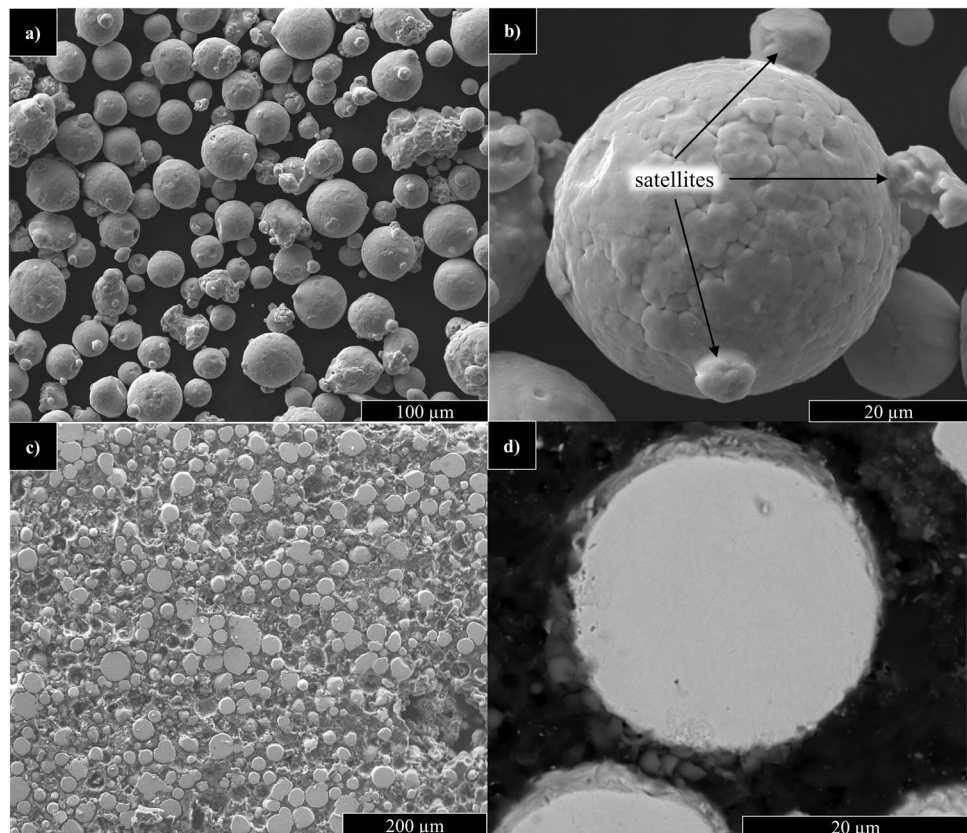
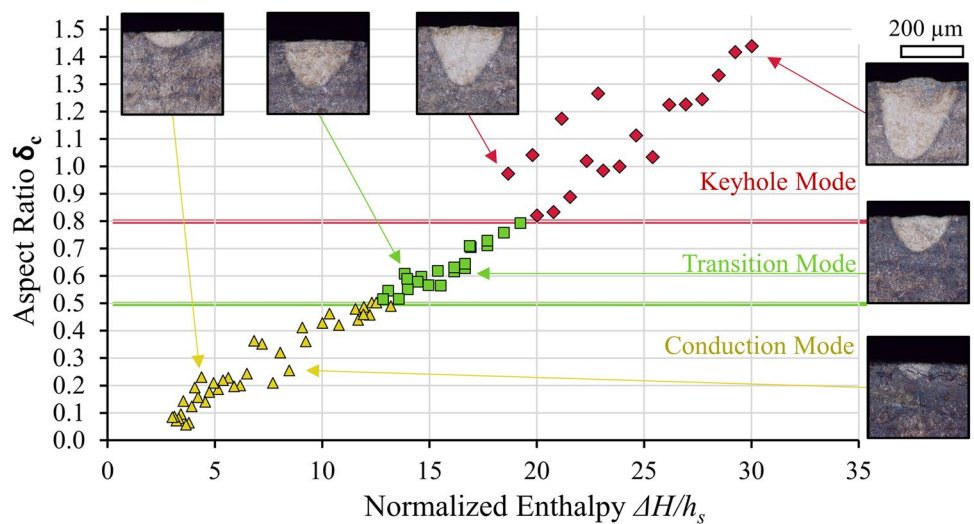


Fig. 5 The corrected aspect ratio δ_c over normalized enthalpy $\frac{\Delta H}{h_s}$ with the threshold between conduction and transition mode at $\delta_c = 0.5$ and the threshold to keyhole mode at $\delta_c = 0.8$



$d_s \geq 0.1$ mm for 800 mm/s. Figure 6d shows for a laser power of 210 W, the change from the conduction mode to transition mode to keyhole mode with increasing normalized enthalpy. The corresponding LOM image for each process parameter combination can be found in the supplementary data. All parameter combinations resulting in transition mode are given in Fig. 7 in the typical plot with laser power versus scan speed.

3.3 LPBF process parameters and density

Table 5 shows the process parameters used for the hatch study. As a result of the single-track experiments, process parameter combinations in the transition mode with values of normalized enthalpy $\frac{\Delta H}{h_s}$ between 9 and 15 were applied. Figure 8 shows the color-coded relative density of the cubic specimens in the chart

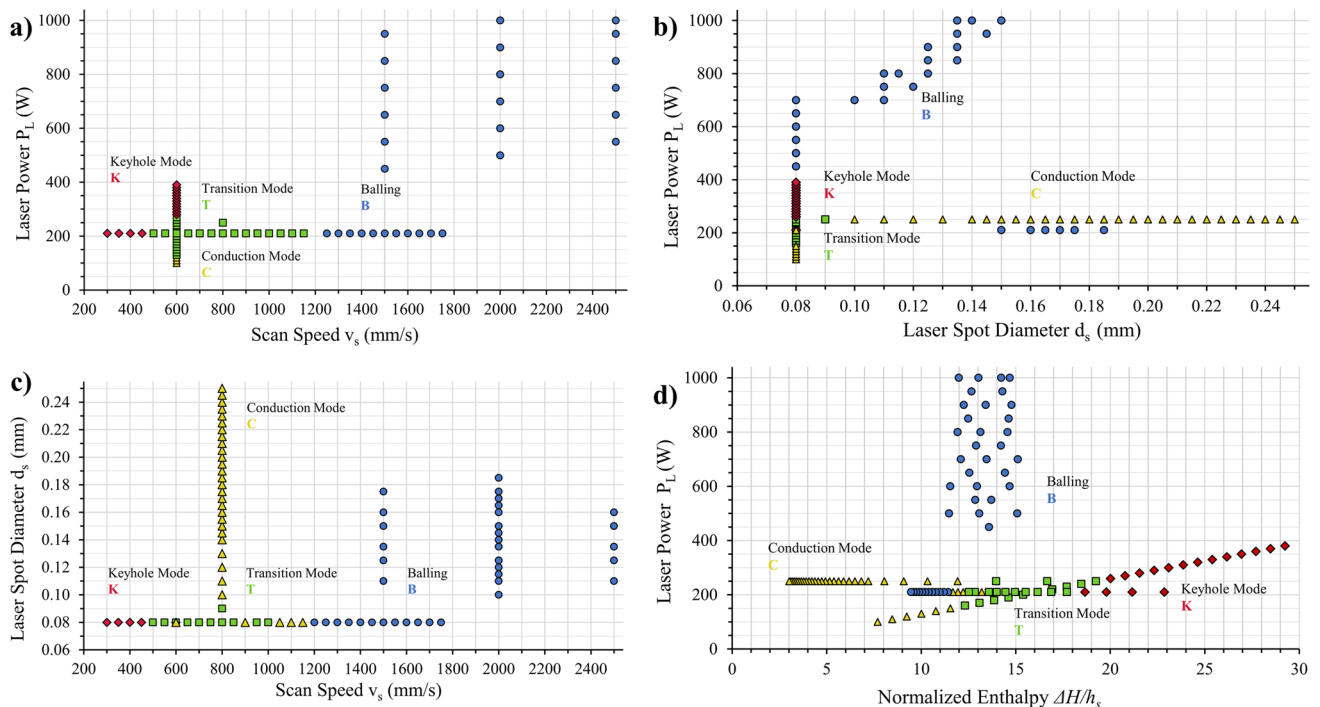
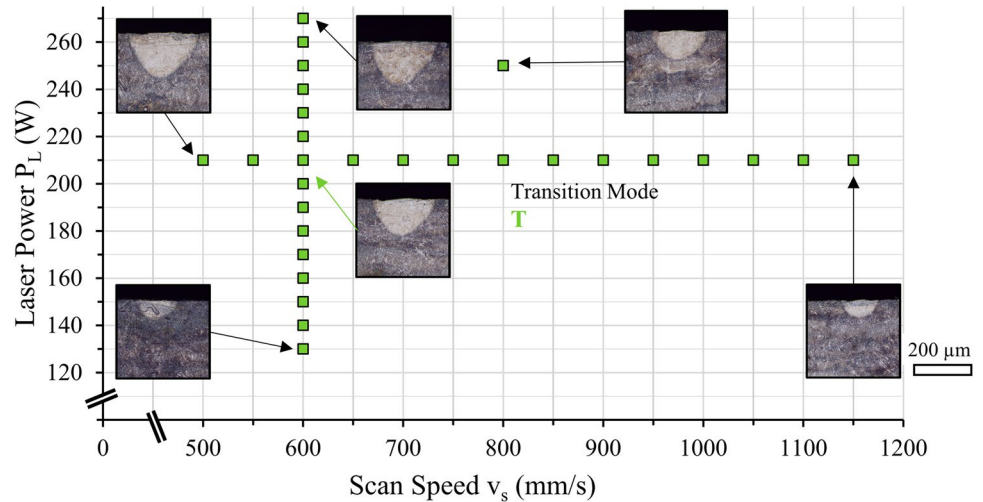


Fig. 6 Overview of the parameter combinations of laser power P_L , scan speed v_s and laser spot diameter d_s from the single-track experiments with the associated melting mode classification in different

plots. **a** Laser power P_L plotted over scan speed v_s , **b** laser power P_L plotted over laser spot diameter d_s , **c** laser spot diameter d_s over scan speed v_s , and **d** laser power P_L over normalized enthalpy $\frac{\Delta H}{h_s}$

Fig. 7 shows the parameter combinations laser power P_L over scan speed v_s that led to single tracks in transition mode. Selected parameters from this region were used to perform the LPBF studies with varying hatch distance h_d



of hatch distance h_d versus normalized enthalpy $\frac{\Delta H}{h_s}$. The highest density, 99.8%, was achieved with a hatch distance of 0.1 mm at a normalized enthalpy of 11.9. Table 5 shows the optimized LPBF parameters that were used for the production of the tensile specimens.

3.4 Mechanical properties and microstructure

Table 6 sums up the mechanical properties of ultimate tensile strength UTS (MPa), elongation at fracture (%), and hardness (HV1) of the tensile specimens produced via LPBF determined in the as-built condition and in the heat-treated condition. Results of the micro-hardness measurements of the polished cross-sections of the single-track experiments of both the untempered martensite and the tempered martensite are listed. Areas of untempered martensite in a single-track number 29 in keyhole mode are shown in SEM in Fig. 9a and in LOM in Fig. 9b. The two areas of the untempered martensite and the tempered martensite separated by the austenitization boundary in LOM at higher magnification are shown in Fig. 9c.

4 Discussion

The low-alloy steel powder E185 of Boehler shows few satellites, no inner porosity, and a spherical particle shape (Fig. 4b and d). The powder exhibits a PSD in the typical

LPBF size range, high flowability, high bulk, and high tap density, and is suitable for processing via LPBF (Table 4).

For a reliable LPBF process and to achieve high densities (Fig. 8), it is essential to avoid keyhole pores, lack of fusion pores, and spatter. Figure 10a shows that when the laser beam irradiates the melt pool, evaporation occurs, causing a recoil pressure. The recoil pressure leads to the depression of the melt pool and is responsible for the formation of keyholes, as shown in Fig. 9a [25]. In combination with the evaporation flux and the local pressure change, induced gas convection of the process gas due to the Bernoulli effect leads to powder deposition, denudation, and cold spatters [26, 27]. In contrast, hot spatters are associated with high melt pool dynamics as they occur at high laser powers and may consist of melt droplets ejected with the vapor [28]. The driving force for melt pool formation is Marangoni convection, which is a mass flow in the opposite direction of the high thermal gradient in the liquid melt [29]. Gas pores in the melt pool are entrained by Marangoni convection, overcoming buoyancy and forcing pores downward from the surface just before solidification [30]. Keyhole pores (Fig. 10b III) form when the keyhole collapses or is closed by surface tension, often at the end of a melt track or scan vector [31, 32].

To date, there have been only a few approaches to the determination of process parameters on the basis of normalized enthalpy or melting mode. Table 7 provides a comprehensive comparison of these studies. The present study is the

Table 5 The parameter range for the LPBF hatch study, density measurements, and the selected parameters

	Laser power P_L (W)	Scan speed v_s (mm/s)	Laser spot diameter d_s (mm)	Hatch distance h_d (mm)	Layer thickness t_1 (mm)	$\frac{\Delta H}{h_s}$
Hatch study	130–260	500–1100	0.08	0.06–0.12	0.03	9.3–14.8
Optimized parameters	210	900	0.08	0.1	0.03	11.9

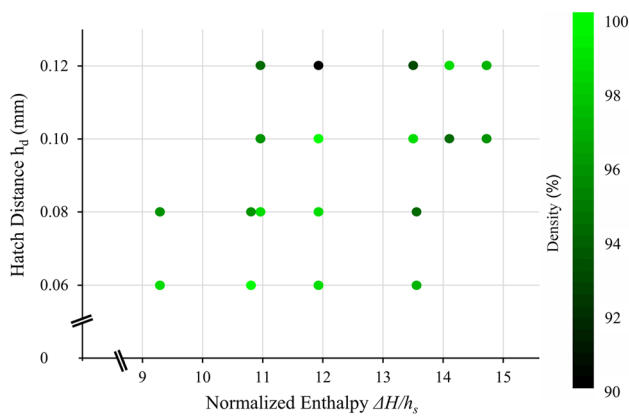


Fig. 8 Relative Archimedean density of cubic LPBF specimens color-coded in the plot of the hatch distance h_d over normalized enthalpy $\frac{\Delta H}{h_s}$ using process parameters from the transition region of the single-track experiments

first to establish this approach for steels, covering a wider range of parameters than the other studies.

Based on scaling laws for additive manufacturing according to Rubenchik et al. [19], melt pool dimensions can be correlated to normalized enthalpy. The work presented shows that normalized enthalpy can be used to effectively determine LPBF process parameters for novel materials and thus avoid process-related defects. Single tracks with varying process parameter combinations were categorized with respect to their melting modes based on the melt pool geometry. According to the welding literature [17, 18, 33], the keyhole and conduction modes are distinguished. Tracks showing features of balling are classified as balling defects, according to [11, 21]. Balling defects can be combined with a lack of fusion defects caused by a melt pool depth or width that is too small, as described in [11, 24]. Melt pools in conduction mode have consistent geometry with low melt dynamics and no spatter but low absorptivity and low penetration depth. The advantages of melting in the keyhole mode are a high absorptivity rate and high penetration depth, but with the drawbacks of high melt pool dynamics, spatter, evaporation, and resulting keyhole pores [22]. In addition to the conduction and keyhole modes, Patel et al. [13] found a regime in between conduction and keyhole mode for LPBF called the transition mode, with $0.5 \leq \delta_c < 0.8$.

The transition mode occurs when the melt pool depths allow multiple reflections, which leads to a higher but fluctuating laser absorptivity [5]. The transition mode is considered desirable in LPBF because the positive effects of conduction and keyhole modes, namely sufficiently consistent melt pool geometry and sufficient penetration depth, can be combined [5]. The fourth category is balling. As previously reported, balling including undercuts (Fig. 3d) can lead to lack of fusion defects [11, 34].

To determine the melt pool dimensions, the solidification and thermal history of the single tracks should be considered. During rapid solidification of the single tracks, γ -austenite transforms to martensite, as proven by the high hardness of 538 HV1 (Table 6). The martensitic structure can be seen in LOM and SEM (Figs. 2 and 9c). Re-austenitization occurs when the material is reheated exceeding the austenitization temperature, leading to a second solid-phase transformation from austenite to martensite. This transformation takes place in the HAZ adjacent to the melt pool. Martensite undergoes a tempering procedure in the area of the HAZ below the austenitization temperature. During tempering, cementite precipitates, which leads to a dark appearance in the LOM micrograph when etched in Nital (Fig. 9b), while the untempered martensite appears light [35]. The boundary between HAZ and the melt pool area can be detected only in the BSE mode, as precipitates of elements with lower atomic numbers, such as C and O, are enriched at the melt pool boundary (Fig. 9a). Thus, the depth of the melt pool e_c can be measured via SEM using BSE. The width of the melt pool d_c can be measured using an FVM based on differing morphologies and elevations, respectively.

Based on e_c and d_c , the aspect ratio δ_c can be calculated and the melting mode determined according to the specification in Sect. 2.2. The absorptivity A strongly depends on the melting mode and increases from conduction to transition to keyhole mode. In conduction mode, A mainly depends on the material-specific absorptivity measured on flat specimens. In transition mode, melt pool depression starts to form due to the increasing recoil pressure caused by evaporating material, resulting in multiple reflections of the laser and, thus, an increase in absorptivity [5], as shown in Fig. 10a. In keyhole mode, a constant absorptivity is established, and the laser beam is trapped inside the deep vaporized regions of the melt pool. Trapp et al.

Table 6 The mechanical properties of the LPBF specimens, tensile strength and hardness of the as-built and heat-treated specimens, and hardness of specimens obtained from the single-track experiments

	Ultimate tensile strength UTS (MPa)	Elongation at fracture (%)	Hardness (HV1)
LPBF as-built	1143 ± 71	12.91 ± 1.12	373 ± 41
LPBF heat-treated	1222 ± 85	11.10 ± 0.91	394 ± 54
single-track untempered martensite			538 ± 6
Single-track tempered martensite			402 ± 9

measured an absorptivity A for SS 316L of approximately 0.3 in conduction mode to almost 0.8 in keyhole mode [36]. According to them, for aspect ratios, as determined in the present work, the respective A amounts to about 0.3 to 0.6. Patel et al. assumed constant absorptivity values for each melting mode for steel and a beam spot radius of $> 47 \mu\text{m}$, with 0.31 for conduction mode, 0.555 for transition mode, and 0.8 for keyhole mode [5]. King et al. used a constant absorptivity A of 0.4 to plot the aspect ratio versus the normalized enthalpy. They reported a linear relation in conduction mode and a significant increase in the trend line slope when reaching the keyhole threshold [22]. Figure 5 shows a linear relation of the aspect ratio and normalized enthalpy when assuming a constant absorptivity A of 0.4 in transition mode. The chart reveals a progressive trend in the keyhole mode, i.e., the values scatter and deviates from this

linearity. In conduction mode, a slightly regressive trend can be observed. The trend changes indicate that the actual absorptivity A for the conduction and keyhole modes deviates slightly from 0.4. In conduction mode, absorptivity A may be slightly lower than 0.4, and in keyhole mode, it may be slightly higher. The model with a constant absorptivity A of 0.4 is considered to be sufficiently precise in the range of the experiments of this work since the analysis of variance showed no significant difference in the residuals from the linearity for each melting mode. Figure 5 identifies a normalized enthalpy in the range from 12 to 20 for melt tracks in transition mode. Figure 6d shows conduction mode, or balling, for all single tracks below a normalized enthalpy of 12 and keyhole mode above a normalized enthalpy of 20. In addition to the normalized enthalpy, further boundary conditions must be considered. Figure 6a

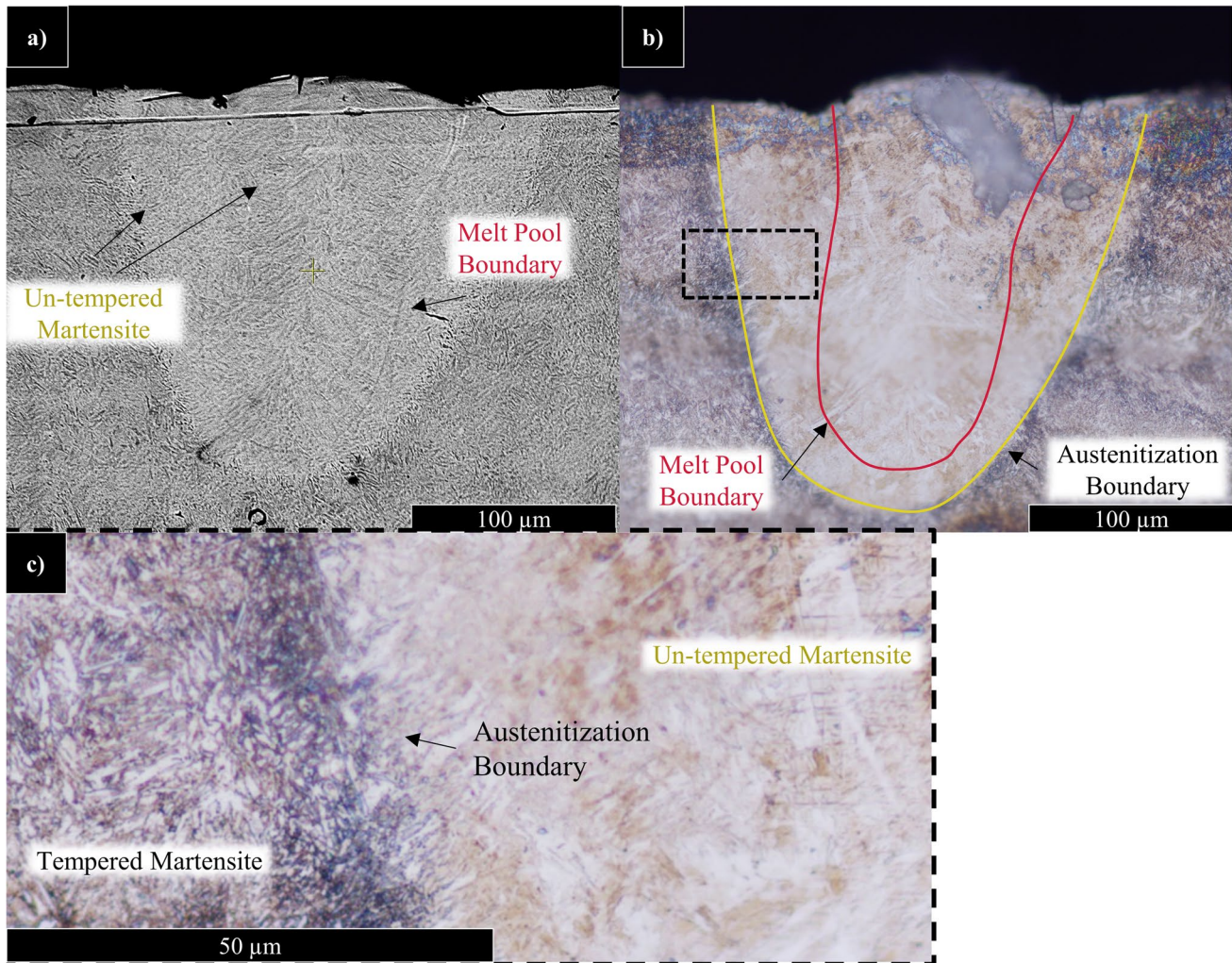
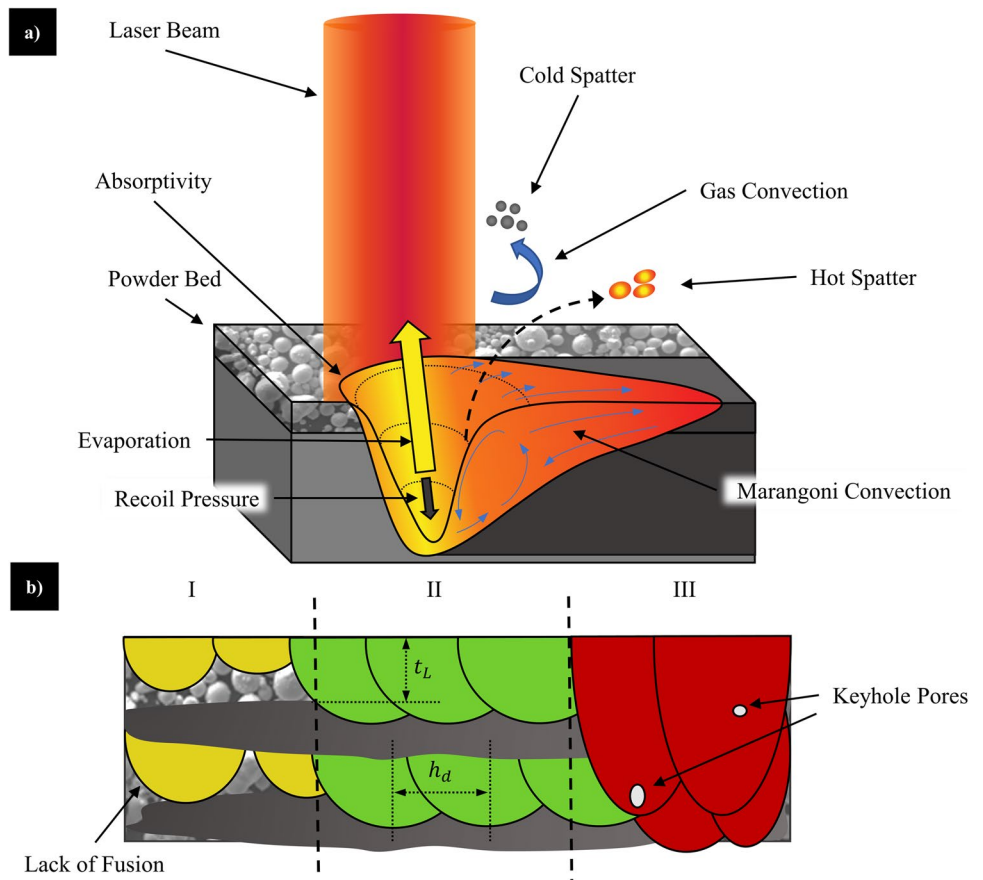


Fig. 9 a SEM micrograph of the single-track number 29 in keyhole mode. b LOM micrograph of the same single-track number, with red line indicating the melt pool boundary and a yellow line indicating the austenitization boundary. The black dashed rectangle indicates the

area magnified in c. c The left side of the LOM micrograph represents darker tempered martensite, the brighter untempered martensite is on the right side, and the transition between the areas is the austenitization boundary

Fig. 10 Schematic illustration of the LPBF process. **a** Laser beam, powder bed, and the melt pool, including the main physical mechanisms and effects. **b** Cross-section of an LPBF part built under different process regimes. I: Lack of fusion, where the depth and width of the melt pool are insufficient and unmelted powder remains. II: Desired conditions as in transition mode. III: Keyhole mode, deep melt tracks with keyhole pores



and c reveal that all single tracks with v_s of 1200 mm/s or more show balling. Balling at high scan speeds caused by Plateau–Rayleigh instability is a well-known phenomenon in LPBF [37]. Leaving the balling defects out of consideration, all single tracks made with laser spot diameters $d_s > 0.1$ mm and with a normalized enthalpy below 12 show conduction mode. When the tracks in conduction mode have too little depth e compared to layer thickness t_l or width d_m compared to hatch distance h_d , there is a lack of fusion defects [24], as shown in Fig. 10b I. To estimate

the lack of fusion defects, the following criteria have to be fulfilled [11, 34]:

- The melt pool depth must reach at least the layer thickness ($e \geq t_l$) (Fig. 10b II)
- The hatch distance must not exceed $h_d \leq d_m \cdot \sqrt{1 - \frac{t_l}{t_l + e}}$

A lack of fusion leads to a significantly lower density. Archimedes’ density measurement can be used to measure the relative density of the LPBF component and thus check

Table 7 Comparison with other recent studies that have used the normalized enthalpy in the LPBF for the determination of the process parameters

Year	Materials	Laser power (W)	Scan speed (mm/s)	Laser spot size (mm)	Type of study
Present study	2023 E185 low-alloy steel	100–1000	300–2500	0.080–0.250	Experimental, calculation
Kosiba et al. [23]	2023 Zr-based alloy	90–120	700–1100	0.050	Experimental, calculation
Weaver et al. [21]	2022 Inconel 625	122–195	200–1200	0.050–0.322	Experimental, calculation
Patel et al. [13]	2022 Ti64, 316L, Inconel 625 AlSi10Mg	150–400	500–1363	0.070–0.200	Experimental, calculation
Tabasi et al. [16]	2020 316L, bronze, red-gold	155–500	200–490	0.065; 0.085	Experimental, simulation
Ye et al. [20]	2019 Ti64, 316L, Inconel 625	25–300	500–1500	0.050–0.100	Experimental, simulation
Rubenchik et al. [19]	2018 Ti64, 316L, Inconel 625	100–500	0–5000	0.040; 0.080	Simulation, calculation

the entire volume for defects. As the normalized enthalpy $\frac{\Delta H}{h_s}$ increases, the melt pool size also increases at a constant laser spot size [21]. For a larger melt pool, the hatch distance h_d can be increased according to the hatch criteria [11]. With a h_d of 100 μm and a normalized enthalpy of 11.9, the highest relative density of 99.8% was achieved in this study (Fig. 8). In the single-track experiments, a normalized enthalpy of 11.9 lies with an aspect ratio of 0.5 on the border between conduction mode and transition mode (Fig. 5). This resulted in the optimized process parameters used for the production of the tensile specimens (Table 6).

The scaling law (Eq. 2) allows estimation of the dimensions of the melt pool and avoidance of balling defects when considering the boundary condition for scan speed. The systematic approach in this work can be used to narrow down the initial selection of LPBF process parameter combinations for novel alloys to reduce the need for highly iterative experiments. In addition, this work can be used to understand the physical origin of defects based on LPBF processing parameters, such as laser power, scan speed, laser spot diameter, and hatch distance. Melt defects, such as lack of fusion defects due to low energy input and spatters or extensive evaporation due to too high energy input, can be avoided to a high extent.

5 Conclusions and outlook

This study covers the systematic approach to optimizing LPBF parameters demonstrated with the low-alloy steel E185. Based on the results, the following conclusions were drawn:

- The achieved mechanical properties of the 99.8% dense specimens using a laser power $P_L = 210$ W, a scan speed $v_s = 900$ mm/s, a laser spot diameter $d_s = 0.08$ mm, a hatch distance $h_d = 0.1$ mm, a layer thickness $t_l = 0.03$ mm, and a scan vector length of 5 mm are the following:
 - o As-built: Tensile strength of 1143 ± 71 MPa, elongation of $12.9 \pm 1.1\%$, and hardness of 373 ± 41 HV1
 - p Heat-treated: Tensile strength of 1233 ± 86 MPa, elongation of $11.1 \pm 0.9\%$, and hardness of 596 ± 14 HV1
- A systematic approach is used to enable the production of defect-free parts for new AM alloys. The proposed framework integrates the normalized enthalpy to determine regions of processing parameters corresponding to different melting modes (conduction, transition, keyhole,

and balling). The main benefit of this approach lies in its ability to determine process windows in an accelerated fashion, eliminating the need for costly and time-consuming comprehensive parameter studies.

- The low-alloy steel E185 was processed via LPBF crack-free with a normalized enthalpy of $\frac{\Delta H}{h_s} = 11.9$, which is in the transition mode region close to the conduction mode.
- Fabricating fully dense as-built specimens is only an initial step toward further objectives for the proposed methodology, such as tailoring the solidification microstructure, which is also dependent on the melt pool geometry [38, 39].
- The methodology proposed in this work has the potential to systematize the optimization of LPBF processing parameters for new alloys and to identify and avoid process-related defects to improve process stability and reliability.
- The applied approach reaches its limits when defects are caused by material-induced defects such as hot cracking or gas pores.
- The melt pool shape can be used not only to define optimized LPBF parameters but also in conjunction with computational materials engineering methods for microstructure simulation, which will be the aim of future work.

Supplementary Information The online version contains supplementary material available at <https://doi.org/10.1007/s00170-023-11377-2>.

Author contribution Simon Bergmüller: conceptualization, methodology, investigation, formal analysis, and writing—original draft. Lorenz Fuchs: methodology and data acquisition. Lukas Gerhold: methodology and data acquisition. Lukas Kaserer: methodology. Gerhard Leichtfried: supervision and writing—review and editing.

Funding Open access funding provided by University of Innsbruck and Medical University of Innsbruck.

Declaration

Competing interests The authors declare no competing interests.

Open Access This article is licensed under a Creative Commons Attribution 4.0 International License, which permits use, sharing, adaptation, distribution and reproduction in any medium or format, as long as you give appropriate credit to the original author(s) and the source, provide a link to the Creative Commons licence, and indicate if changes were made. The images or other third party material in this article are included in the article's Creative Commons licence, unless indicated otherwise in a credit line to the material. If material is not included in the article's Creative Commons licence and your intended use is not permitted by statutory regulation or exceeds the permitted use, you will need to obtain permission directly from the copyright holder. To view a copy of this licence, visit <http://creativecommons.org/licenses/by/4.0/>.

References

1. Yadroitsev I, Yadroitsava I, du Plessis A, MacDonald E (2021) Fundamentals of laser powder bed fusion of metals. Elsevier. <https://doi.org/10.1016/c2020-0-01200-4>
2. Ahmed N, Barsoum I, Haidemenopoulos G, Al-Rub RKA (2022) Process parameter selection and optimization of laser powder bed fusion for 316L stainless steel: a review. *J Manuf Process* 75:415–434. <https://doi.org/10.1016/J.JMAPRO.2021.12.064>
3. Sabooni S, Chabok A, Feng SC, Blaauw H, Pijper TC, Yang HJ, Pei YT (2021) *Addit Manuf* 46:102176. <https://doi.org/10.1016/J.ADDMA.2021.102176>
4. Wei S, Kumar P, Lau KB, Wu D, Liew LL, Wei F, Teo SL, Cheong A, Ng CK, Zhang B, Tan CC, Wang P, Ramamurthy U (2022) Effect of heat treatment on the microstructure and mechanical properties of 2.4 GPa grade maraging steel fabricated by laser powder bed fusion. *Addit Manuf* 59:103190. <https://doi.org/10.1016/J.ADDMA.2022.103190>
5. Oliveira JP, LaLonde AD, Ma J (2020) Processing parameters in laser powder bed fusion metal additive manufacturing. *Mater. Des.* 193:108762. <https://doi.org/10.1016/j.matdes.2020.108762>
6. Aumayr C, Platl J, Zunko H, Turk C (2020) Additive manufacturing of a low-alloyed engineering steel additive Fertigung eines niedriglegierten Einsatzstahls. *BHM Berg- Huettenmaenn Monatsh* 165:137–142. <https://doi.org/10.1007/s00501-020-00966-3>
7. voestalpine BÖHLER Edelstahl GmbH & Co KG (2021) Pulver für die additive fertigung: E185 AMPO/Fe-Basislegierungen - material data sheet. <https://www.boehler-edelstahl.com/de/products/e185ampo/>. Accessed 16 Jan 2023
8. voestalpine Stahl GmbH (2023) Additive manufacturing for the automotive industry (web page). <https://www.voestalpine.com/ultralights/en/Newsletter/All-Automotive-Notes-articles/Additive-manufacturing-for-the-automotive-industry>. Accessed 13 March 2023
9. GKN Powder Metallurgy (2022) Low alloy steels for additive manufacturing (web page). <https://www.gknp.com/en/our-businesses/gkn-additive/low-alloy-steels-for-additive-manufacturing/>. Accessed 13 March 2023
10. Seede R, Zhang B, Whitt A, Picak S, Gibbons S, Flater P, Elwany A, Arroyave R, Karaman I (2021) Effect of heat treatments on the microstructure and mechanical properties of an ultra-high strength martensitic steel fabricated via laser powder bed fusion additive manufacturing. *Addit Manuf* 47:102255. <https://doi.org/10.1016/J.ADDMA.2021.102255>
11. Zhang B, Seede R, Xue L, Atli KC, Zhang C, Whitt A, Karaman I, Arroyave R, Elwany A (2021) An efficient framework for printability assessment in laser powder bed fusion metal additive manufacturing. *Addit Manuf* 46:102018. <https://doi.org/10.1016/j.addma.2021.102018>
12. Cui X, Zhang S, Zhang CH, Chen J, Zhang JB, Dong SY (2021) Additive manufacturing of 24CrNiMo low alloy steel by selective laser melting: influence of volumetric energy density on densification, microstructure and hardness. *Mater Sci Eng A* 809:140957. <https://doi.org/10.1016/J.MSEA.2021.140957>
13. Patel S, Vlasea M (2020) Melting modes in laser powder bed fusion. *Materialia* 9:100591. <https://doi.org/10.1016/j.mtla.2020.100591>
14. Mukherjee T, Manvatkar V, De A, DebRoy T (2017) Dimensionless numbers in additive manufacturing. *J Appl Phys* 121:064904. <https://doi.org/10.1063/1.4976006>
15. Xie X, Samaei A, Guo J, Liu WK, Gan Z (2022) Data-driven discovery of dimensionless numbers and governing laws from scarce measurements. *Nat Commun* 2022 13:1. 13 1–11. <https://doi.org/10.1038/s41467-022-35084-w>
16. Ghasemi-Tabasi H, Jhabvala J, Boillat E, Ivas T, Drissi-Daoudi R, Logé RE (2020) An effective rule for translating optimal selective laser melting processing parameters from one material to another. *Addit Manuf* 36:101496. <https://doi.org/10.1016/j.addma.2020.101496>
17. Fabbro R (2019) Scaling laws for the laser welding process in keyhole mode. *J Mater Process Technol* 264:346–351
18. Hann DB, Iammi J, Folkes J (2010) Keyholing or conduction - prediction of laser penetration depth, in: *Proc. 36th Int. MATA-DOR Conf.*, Springer London 275–278. https://doi.org/10.1007/978-1-84996-432-6_63
19. Rubenchik AM, King WE, Wu SS (2018) Scaling laws for the additive manufacturing. *J Mater Process Technol* 257:234–243. <https://doi.org/10.1016/j.jmatprotec.2018.02.034>
20. Ye J, Khairallah SA, Rubenchik AM, Crumb MF, Guss G, Belak J, Matthews MJ (2019) Energy coupling mechanisms and scaling behavior associated with laser powder bed fusion additive manufacturing. *Adv Eng Mater* 21:1900185. <https://doi.org/10.1002/adem.201900185>
21. Weaver JS, Heigel JC, Lane BM (2022) Laser spot size and scaling laws for laser beam additive manufacturing. *J Manuf Process* 73:26–39. <https://doi.org/10.1016/j.jmapro.2021.10.053>
22. King WE, Barth HD, Castillo VM, Gallegos GF, Gibbs JW, Hahn DE, Kamath C, Rubenchik AM (2014) Observation of keyhole-mode laser melting in laser powder-bed fusion additive manufacturing. *J Mater Process Technol* 214:2915–2925. <https://doi.org/10.1016/J.JMATPROTEC.2014.06.005>
23. Kosiba K, Kononenko DY, Chernyavsky D, Deng L, Bednarcik J, Han J, van den Brink J, Kim HJ, Scudino S (2023) Maximizing vitrification and density of a Zr-based glass-forming alloy processed by laser powder bed fusion. *J Alloys Compd* 940:168946. <https://doi.org/10.1016/j.jallcom.2023.168946>
24. Gaikwad A, Giera B, Guss GM, Forien JB, Matthews MJ, Rao P (2020) Heterogeneous sensing and scientific machine learning for quality assurance in laser powder bed fusion – a single-track study. *Addit Manuf* 36:101659. <https://doi.org/10.1016/j.addma.2020.101659>
25. Tsubouchi K, Furumoto T, Yamaguchi M, Ezura A, Yamada S, Osaki M, Sugiyama K (2022) Evaluation of spatter particles, metal vapour jets, and depressions considering influence of laser incident angle on melt pool behaviour. *Int J Adv Manuf Technol* 120:1821–1830. <https://doi.org/10.1007/S00170-022-08887-W/FIGURES/12>
26. Kaserer L, Bergmueller S, Braun J, Leichtfried G (2020) Vacuum laser powder bed fusion—track consolidation, powder denudation, and future potential. *Int J Adv Manuf Technol* 110:3339–3346. <https://doi.org/10.1007/s00170-020-06071-6>
27. Matthews MJ, Guss G, Khairallah SA, Rubenchik AM, Depond PJ, King WE (2016) Denudation of metal powder layers in laser powder bed fusion processes. *Acta Mater* 114:33–42. <https://doi.org/10.1016/j.actamat.2016.05.017>
28. Ly S, Rubenchik AM, Khairallah SA, Guss G, Matthews MJ (2017) Metal vapor micro-jet controls material redistribution in laser powder bed fusion additive manufacturing. *Sci Rep* 7. <https://doi.org/10.1038/s41598-017-04237-z>
29. Guo Q, Zhao C, Qu M, Xiong L, Hojjatzadeh SMH, Escano LI, Parab ND, Fezzaa K, Sun T, Chen L (2020) In-situ full-field mapping of melt flow dynamics in laser metal additive manufacturing. *Addit Manuf* 31. <https://doi.org/10.1016/j.addma.2019.100939>
30. Martin AA, Caltan NP, Hammons JA, Khairallah SA, Nielsen MH, Shuttlesworth RM, Sinclair N, Matthews MJ, Jeffries JR, Willey TM, Lee JRI (2019) Ultrafast dynamics of laser-metal interactions in additive manufacturing alloys captured by in situ X-ray imaging. *Mater Today Adv* 1:100002. <https://doi.org/10.1016/j.mtadv.2019.01.001>

31. Huang Y, Fleming TG, Clark SJ, Marussi S, Fezzaa K, Thiyagal-ingam J, Leung CLA, Lee PD (2022) Keyhole fluctuation and pore formation mechanisms during laser powder bed fusion additive manufacturing. *Nat Commun* 13:1–11. <https://doi.org/10.1038/s41467-022-28694-x>
32. Qu M, Guo Q, Escano LI, Clark SJ, Fezzaa K, Chen L (2022) Mitigating keyhole pore formation by nanoparticles during laser powder bed fusion additive manufacturing. *Addit Manuf Lett* 3:100068. <https://doi.org/10.1016/j.addlet.2022.100068>
33. Lankalapalli KN, Tu JF, Gartner M (1996) A model for estimating penetration depth of laser welding processes. *J Phys D Appl Phys* 29:1831. <https://doi.org/10.1088/0022-3727/29/7/018>
34. Seede R, Shoukr D, Zhang B, Whitt A, Gibbons S, Flater P, Elwany A, Arroyave R, Karaman I (2020) An ultra-high strength martensitic steel fabricated using selective laser melting additive manufacturing: densification, microstructure, and mechanical properties. *Acta Mater* 186:199–214. <https://doi.org/10.1016/j.actamat.2019.12.037>
35. Petzow G (2006) *Metallographisches, keramographisches und plastographisches Ätzen*, Schweizerbart Science Publishers, Stuttgart, Germany. http://www.schweizerbart.de/publications/detail/isbn/9783443230166/Petzow_Metall_Keram_u_Plastogr_Atz. Accessed 16 Jan 2023
36. Trapp J, Rubenchik AM, Guss G, Matthews MJ (2017) In situ absorptivity measurements of metallic powders during laser powder-bed fusion additive manufacturing. *Appl Mater Today* 9:341–349. <https://doi.org/10.1016/J.APMT.2017.08.006>
37. Wang W, Liang SY (2022) Prediction of molten pool height, contact angle, and balling occurrence in laser powder bed fusion. *Int J Adv Manuf Technol* 119:6193–6202. <https://doi.org/10.1007/s00170-021-08633-8>
38. Köhnen P, Ewald S, Schleifenbaum JH, Belyakov A, Haase C (2020) Controlling microstructure and mechanical properties of additively manufactured high-strength steels by tailored solidification. *Addit Manuf* 35:101389. <https://doi.org/10.1016/j.addma.2020.101389>
39. Körner C, Helmer H, Bauereiß A, Singer RF (2014) Tailoring the grain structure of IN718 during selective electron beam melting. *MATEC Web Conf* 14:08001. <https://doi.org/10.1051/mateconf/20141408001>

Publisher's Note Springer Nature remains neutral with regard to jurisdictional claims in published maps and institutional affiliations.